

Thermoelectric transport in Ru₂TiSi full-Heusler compounds

Fabian Garmroudi,^{1,*} Michael Parzer,¹ Takao Mori,^{2,3} Andrej Pustogow,¹ and Ernst Bauer¹

¹*Institute of Solid State Physics, TU Wien, 1040 Vienna, Austria*

²*International Center for Materials Nanoarchitectonics (WPI-MANA),*

National Institute for Materials Science, Tsukuba 305-0044, Japan

³*University of Tsukuba, Tsukuba 305-8577, Japan*

Heusler compounds with six valence electrons per atom have attracted interest as thermoelectric materials owing to their semimetallic and semiconducting properties. Here, we theoretically and experimentally investigate electronic transport in Ru₂TiSi-based full-Heuslers. We show that electronic transport in this system can be well captured by a two-parabolic band model. The larger band gap of Ru₂TiSi promises a higher thermoelectric performance, compared to its isovalent family member Fe₂VAl, which has been studied as a thermoelectric material for over two decades. Additionally, we identify *p*-type Ru₂TiSi as far more efficient than previously studied *n*-type compounds and demonstrate that this can be traced back to much lighter and more mobile holes originating from dispersive valence bands. Our findings demonstrate that an exceptionally high dimensionless figure of merit $zT > 1$ can be realized in these *p*-type compounds around 700 K upon proper reduction of the lattice thermal conductivity, *e.g.*, by substituting Zr or Hf for Ti.

I. INTRODUCTION

Heusler compounds represent a highly tunable material platform encompassing over thousand different members that exhibit a variety of interesting electronic phases, ranging from half-metallicity to semiconducting states and nontrivial topological band structures [1–3]. Heusler compounds are typically subcategorized into half-Heuslers (hHs) and full-Heuslers (fHs) with XYZ and X₂YZ stoichiometries, respectively. In half-Heuslers, crystallizing in the non-centrosymmetric C1_b structure (space group no. 216, F43m), one of the X sublattices is vacant, whereas the full-Heusler structure with L1₂ ordering (space group no. 225, Fm3m) can be interpreted as four interpenetrating *fcc* sublattices, two of which are comprised of X atoms, while the others are built-up from the Y and Z atoms. X and Y atoms are usually transition metals, whereas Z is typically a IIIrd, IVth or even Vth main group element [1].

In general, research on Heusler materials is guided by simple electron counting rules, like the Slater-Pauling rule [1, 4–6], which states that Heusler compounds with an average valence electron concentration (VEC) of 6 valence electrons per atom are non-magnetic semiconductors or semimetals, depending on the strength of hybridization. However, as the VEC increases or decreases, magnetic metals emerge. Although there are few exceptions to this [7, 8], hundreds of hH and fH compounds align with this concept and researchers have adhered to these straightforward electron counting rules, as they enable an accurate and quick estimate of the electronic and magnetic ground state properties and serve as fundamental principles [1], particularly in the quest for thermoelectric semiconductors [9–12].

The performance of thermoelectric materials is evaluated by the dimensionless figure of merit $zT = S^2\sigma\kappa^{-1}T$,

which depends on the Seebeck coefficient S , the electrical conductivity σ the thermal conductivity κ and the absolute temperature T , and directly determines the efficiency of a thermoelectric conversion device. For practical purposes, $zT > 1$ is commonly considered as a threshold [13]. While numerous hH compounds, *e.g.* (Ti,Zr,Hf)NiSn, (Nb,Ta)FeSb, etc., are already widely recognized as efficient thermoelectric materials [14–16], their fH relatives have not yet reached zT values, that would make them competitive with state-of-the-art materials [17].

Fe₂VAl is unarguably the most prominent fH thermoelectric material with attractive near-room temperature thermoelectric properties [18–20]. Despite consisting only of metallic elements, Fe₂VAl is a semimetal with a tiny band overlap or an almost gapless semiconductor [21–23]. There are two primary factors limiting the performance of Fe₂VAl thermoelectrics: (i) Their intrinsic

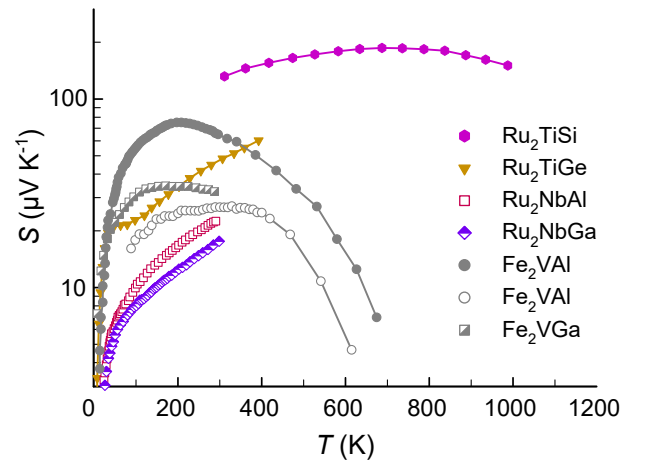


FIG. 1. Comparison of temperature-dependent Seebeck coefficient of various semimetallic and semiconducting full-Heuslers with six valence electrons per atom (VEC = 6).

* f.garmroudi@gmx.at

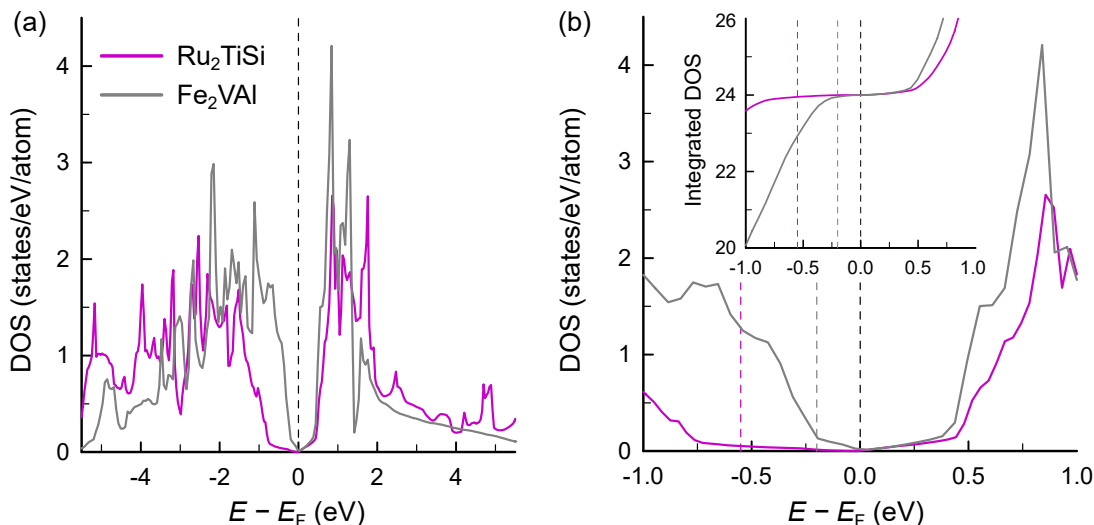


FIG. 2. **Electronic density of states of the full-Heusler compounds Ru_2TiSi and Fe_2VAI .** (a) A deep pseudogap with an almost negligibly small DOS at the Fermi level is present in both compounds, which is framed by sharp features in the DOS, originating from rather localized Fe-3d and Ru-4d states. (b) A close-up around the Fermi energy emphasizes that the pseudogap is much broader in Ru_2TiSi . Additionally, it can be seen that the dispersive pseudogap states, reaching into the gap region (small DOS), especially the valence band states, have a much larger bandwidth and are therefore even more dispersive for Ru_2TiSi compared to Fe_2VAI . Black dashed line indicates the Fermi energy E_F , and grey and purple dashed lines show E_F for a rigid-band doping scenario with 0.05 holes per formula unit. Inset shows the integrated DOS of both compounds.

cally large lattice thermal conductivity and (ii) the small band gap, which results in bipolar conduction already at $T \lesssim 300$ K. Fig. 1 compares the temperature-dependent Seebeck coefficient $S(T)$ of various fH compounds with $\text{VEC} = 6$, reported and experimentally studied in the literature previously [24–28]. Note the pronounced maximum in $S(T)$ of Fe_2VAI at around 200 K, arising from the aforementioned bipolar conduction, *i.e.*, the activation of minority carriers across the narrow band gap. On the other hand, isovalent Ru_2TiSi , a novel fH compound recently studied by Fujimoto *et al.* [28], displays a much larger Seebeck coefficient and broad maximum, vastly surpassing all other known fH compounds over the entire temperature range. This motivated us to experimentally and theoretically study in detail the electronic transport in Ru_2TiSi and assess its potential thermoelectric performance at optimized doping.

II. EXPERIMENTAL METHODS AND MODELLING

Polycrystalline $\text{Ru}_2\text{TiSi}_{1-x}\text{Al}_x$ materials were synthesized by melting raw elements with high purity (99.99% Ru, 99.95% Ti, 99.9999% Si and 99.999% Al) using a high-frequency induction heating furnace. Even though powder X-ray diffraction investigations displayed a single Heusler phase directly after the melting procedure, the samples were further annealed at 1273 K for two days in vacuum (10^{-5} mbar) to optimize homogeneity. The samples were then cut using a high-speed cutting device (Accutom by the company Struers) equipped with a di-

amongd cutting wheel. The electrical resistivity and Seebeck coefficient at high temperatures were measured in the temperature range 300–860 K in an inert He atmosphere using a commercially available setup (ZEM3 by ULVAC-RIKO). To analyze the temperature- and carrier concentration-dependent Seebeck coefficient, we employed a least squares fit model based on Boltzmann transport theory and the parabolic band approximation, as implemented in the *SeeBand* software [29]. Within this framework, thermoelectric transport is modelled by numerically solving the respective Fermi transport integrals and summing up the contributions of the individual bands, assuming parallel conduction through two transport channels, *i.e.*, one valence and one conduction band.

III. RESULTS AND DISCUSSION

A. Ru_2TiSi versus Fe_2VAI

In order to understand the thermoelectric properties and enhanced performance of Ru_2TiSi , a natural question would be what distinguishes it from the archetypal thermoelectric fH compound Fe_2VAI . Fig. 2(a) shows the electronic density of states (DOS) of Ru_2TiSi and Fe_2VAI [45]. Both compounds display a deep, well pronounced pseudogap at the Fermi energy E_F , although the gap is significantly broader for Ru_2TiSi . Similar to Fe_2VAI , the DOS of Ru_2TiSi is characterized by sharp peaks (owing to the rather localized Ru-4d states) rising next to both edges of the pseudogap, which results

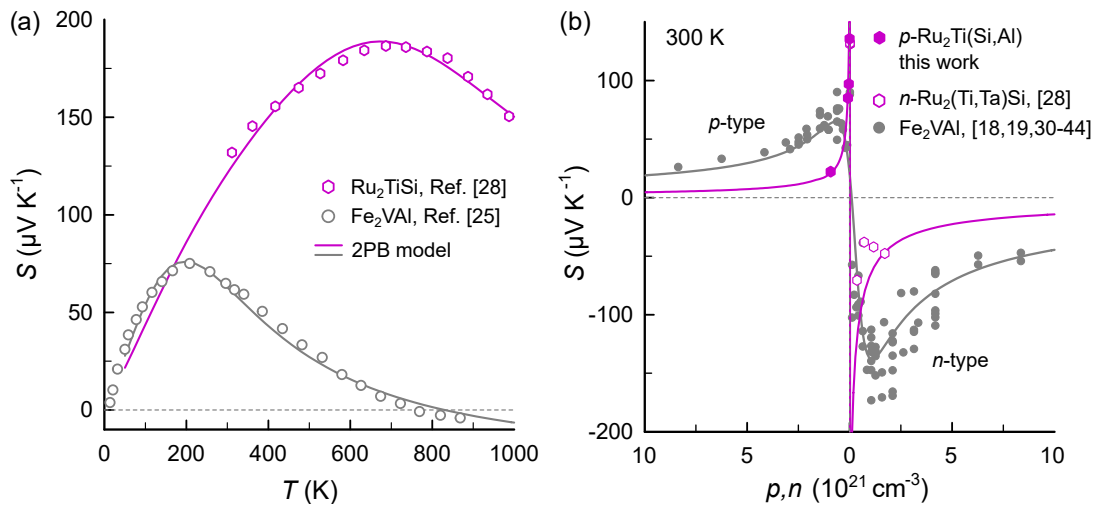


FIG. 3. **Modelling of thermoelectric transport in Fe_2VAI and Ru_2TiSi full-Heuslers.** (a) Comparison of the temperature-dependent Seebeck coefficient of Fe_2VAI and Ru_2TiSi . Experimental data were taken from Refs. [25] and [28], respectively. Solid lines are least-squares fits employing a two-parabolic band model, which excellently captures the temperature-dependent $S(T)$ of both compounds in the entire temperature range. (b) Doping concentration-dependent Seebeck coefficient of p - and n -doped Fe_2VAI and Ru_2TiSi at room temperature. The Seebeck coefficient decreases much more rapidly as a function of the carrier concentration for the latter, indicating that doping is far more efficient in Ru_2TiSi compared to Fe_2VAI , owing to the much lighter and more dispersive bands; p -type $\text{Ru}_2\text{TiSi}_{1-x}\text{Al}_x$ -based compounds (open symbols) were synthesized and investigated in this work. Filled purple symbols were taken from [28] and filled grey symbols were taken from various literature studies [18, 19, 30–44].

in a large differential DOS. Additionally, there are much more dispersive states (with a small DOS) dangling into the gap region, hereafter referred to as *pseudogap states*. It was shown in previous studies that in Fe_2VAI , electronic transport is almost exclusively governed by these pseudogap states. Fig. 2(b) shows the DOS around E_F and a close-up of these pseudogap states. One immediately notices that the pseudogap states are much broader and the DOS much smaller for Ru_2TiSi than for Fe_2VAI , especially at $E < E_F$. This implies much lighter, more mobile charge carriers when E_F is placed in the vicinity of these states. Moreover, the lower density of states effective mass m_{DOS}^* suggests a much more efficient doping scenario for Ru_2TiSi . We illustrate this, by drawing and comparing the Fermi level of hole-doped Fe_2VAI (grey dashed line) and Ru_2TiSi (purple dashed line) for a hole doping concentration of 0.05 holes per formula unit, assuming rigid-band doping. This corresponds approximately to the concentration, for which p -type Fe_2VAI displays its optimal thermoelectric performance. It can be seen that, while for Fe_2VAI , this would place E_F about 0.2 eV below the valence band edge, E_F is shifted by almost 0.6 eV into the valence band for Ru_2TiSi . Hence, a significantly smaller number of holes has to be doped to reach optimal performance (compare also the integrated DOS in the inset of Fig. 2(b)). Interestingly, the difference in m_{DOS}^* appears less sizeable for the conduction band at $E > E_F$.

Fig. 3(a,b) displays the temperature-dependent and doping concentration-dependent Seebeck coefficient ($S(T)$, $S(p, n)$), respectively. In Fig. 3(a), we model ex-

perimental $S(T)$ data of Fe_2VAI and Ru_2TiSi available in the literature [25, 28], by employing a two-parabolic band (2PB) least-squares fit model as implemented in the *SeeBand* software package [29]. To fit the data, three independent fit parameters are adjusted: (i) The position of the Fermi level, (ii) the band gap/overlap E_g and (iii) a weighting parameter $\epsilon_m = (N_{\text{VB}} m_{\text{CB}}^*) / (N_{\text{CB}} m_{\text{VB}}^*)$, which includes degeneracies N_i and effective masses m_i of the two bands ($i = \{\text{VB}, \text{CB}\}$). E_F determines the slope of $S(T)$ at low temperatures, E_g the maximum Seebeck coefficient S_{max} as well as the temperature of the maximum T_{max} , and ϵ dictates the sharpness of the maximum, that is, the tail of $S(T)$ in the bipolar regime at temperatures above T_{max} . Details regarding the modelling framework, which we previously successfully applied to a number of fH [19, 43] and skutterudite thermoelectric materials [46], are described in Ref. [29]. Like for Fe_2VAI , excellent agreement with experimental data is also found for Ru_2TiSi . The somewhat similar slope of $S(T)$ at low temperatures for Fe_2VAI and the extrapolated curve of the 2PB model for Ru_2TiSi indicates a comparable position of E_F with respect to the valence band edge. The most notable difference, however, is that S_{max} is shifted towards much higher temperatures in Ru_2TiSi and reaches a very broad maximum of almost $200 \mu\text{V K}^{-1}$, as opposed to only $70\text{--}80 \mu\text{V K}^{-1}$ in Fe_2VAI .

Fig. 3(b) shows the room-temperature Seebeck coefficient as a function of the hole (p) and electron (n) doping concentration, calculated from the VEC via $p, n = 16 \cdot \text{VEC} / a^3$, where a^3 denotes the cubic unit cell volume of Ru_2TiSi or Fe_2VAI and $16 \cdot \text{VEC}$ represents the number

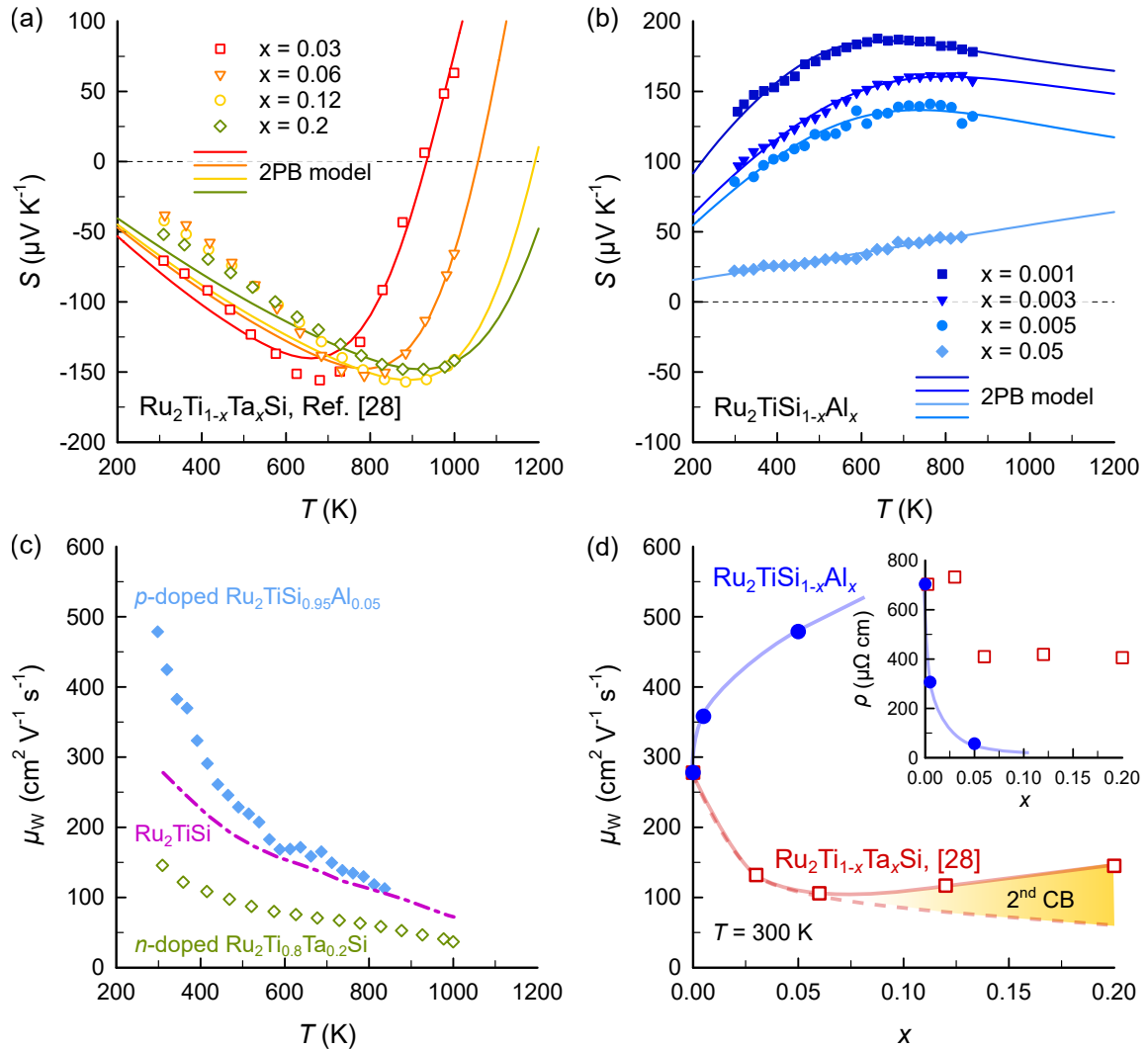


FIG. 4. **Electron-hole band asymmetry in Ru_2TiSi .** Temperature-dependent Seebeck coefficient $S(T)$ of (a) n -type $\text{Ru}_2\text{Ti}_{1-x}\text{Ta}_x\text{Si}$ from Ref. [28] and (b) p -type $\text{Ru}_2\text{TiSi}_{1-x}\text{Al}_{1-x}$ from this work. Solid lines are least-squares fits employing a two-parabolic band model. Notably, the maximum in $|S(T)|$ is much sharper for n -type $\text{Ru}_2\text{Ti}_{1-x}\text{Ta}_x\text{Si}$ and even a sign reversal of the Seebeck coefficient takes place, once minority carriers from the valence band are activated. This implies that holes are much more mobile than carriers occupying the conduction band states in Ru_2TiSi . For p -type $\text{Ru}_2\text{TiSi}_{1-x}\text{Al}_{1-x}$ the maximum in $|S(T)|$ is much broader and doping is much more efficient, that is, a substitution of only a few at.% Al for Si results in a strong decrease of $S(T)$ as E_F moves rapidly away from the band edge. (c) Weighted mobility comparison of heavily n -doped $\text{Ru}_2\text{Ti}_{0.8}\text{Ta}_{0.2}\text{Si}$, pristine Ru_2TiSi and heavily p -doped $\text{Ru}_2\text{TiSi}_{0.95}\text{Al}_{0.05}$. (d) shows the composition-dependent weighted mobility evaluated at 300 K. Solid and dashed lines are a guide to the eye with the yellow area corresponding to an expected gain in μ_w arising from the contribution of a second conduction band. Most importantly, μ_w is much greater for p -type Ru_2TiSi , confirming its superiority over n -type Ru_2TiSi . Inset shows the corresponding composition-dependent resistivity.

of valence electrons in the unit cell. Each point refers to a different sample with a different VEC, which was varied through aliovalent element substitution. Data points were taken from numerous doping studies in the literature and p -type $\text{Ru}_2\text{TiSi}_{1-x}\text{Al}_x$ compounds were synthesized and investigated in the course of this work. Solid lines are theoretical calculations employing a 2PB model. Anand *et al.* previously showed that the $S(p, n)$ dependence of Fe_2VAl can be adequately described employing a 2PB model, assuming a small positive band gap of

$E_g \approx 0.02$ eV and valence and conduction band effective masses of $m_{\text{VB}}^* \approx 4.7 m_e$ and $m_{\text{CB}}^* \approx 12.8 m_e$, respectively [22].

Contrary to Fe_2VAl , we find from our temperature- and doping-dependent analysis of the Seebeck coefficient of Ru_2TiSi a much larger band gap of $E_g \approx 0.22 - 0.24$ eV and much lighter effective masses $m_{\text{VB}}^* \approx 1.0 m_e$ and $m_{\text{CB}}^* \approx 3.3 m_e$. The effect of the latter is directly visible in the much more rapid decrease of S as p, n increase and is consistent with the smaller DOS and broader

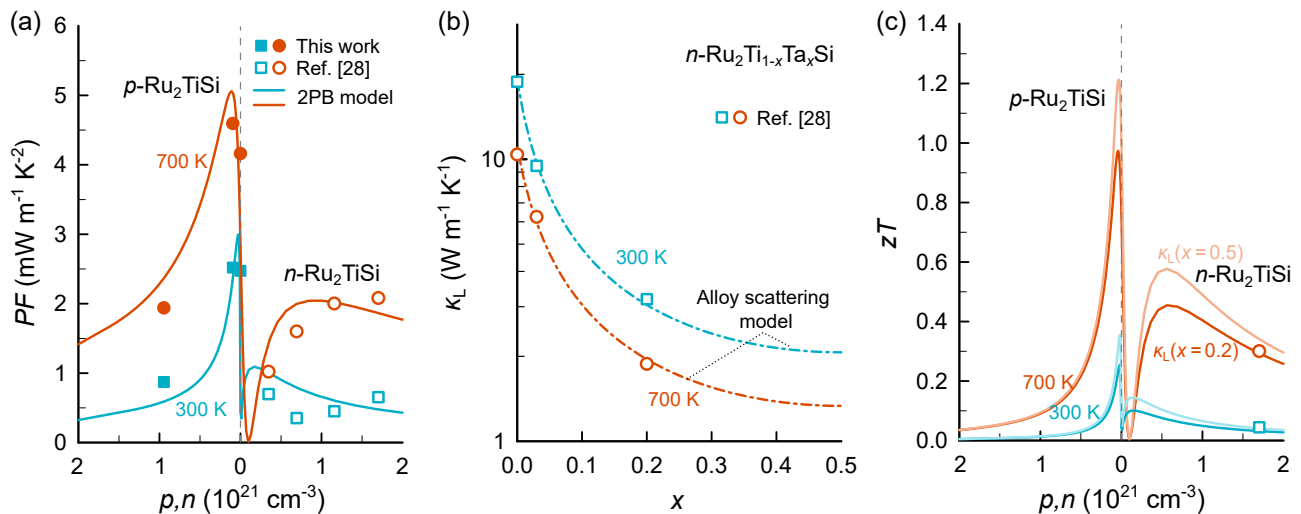


FIG. 5. **Modelling and estimation of thermoelectric performance in Ru₂TiSi-based full-Heusler compounds.** (a) Doping concentration-dependent power factor PF of Ru₂TiSi at 300 K and 700 K. Open and filled symbols are experimental data from this work and from Ref. [28], respectively. Solid lines are theoretical calculations using a two-parabolic band model. A more than two times larger PF is predicted (and experimentally achieved) for p -type Ru₂TiSi due to the superior quality of the valence band structure. (b) Composition-dependent trend of lattice thermal conductivity for Ru₂Ti_{1-x}Ta_xSi from Ref. [28]. Dashed-dotted lines were calculated employing a simple alloy scattering model [22]. The large mass and volume fluctuations imposed by the substitution with heavy $5d$ elements effectively scatter high-frequency heat-carrying phonons. (c) Doping concentration-dependent zT of Ru₂TiSi at 300 K and 700 K. The power factor and the electronic contribution to the thermal conductivity were calculated employing a two-parabolic band model. The lattice thermal conductivity was estimated from (b) under the reasonable assumption that the substitution with other $5d$ elements, such as Hf/Ti, results in a similar suppression of κ_L . Hf substitution does not change the total number of valence electrons and, therefore, remains near the predicted maximum zT , exceeding $zT = 1$ at 700 K, especially in the case that a full solid-solution between Ru₂TiSi and Ru₂HfSi is possible.

bandwidth of the pseudogap states of Ru₂TiSi shown in Fig. 2(b). For p -type Ru₂TiSi_{1-x}Al_x, for instance, $S(300 \text{ K})$ decreases from $130 \mu\text{V K}^{-1}$ in pristine Ru₂TiSi down to only $22 \mu\text{V K}^{-1}$ for $x = 0.05$. In this sense, the valence band electronic structure of Ru₂TiSi appears much more similar to chalcogenide semiconductors, such as Bi₂Te₃ and PbTe, where the underlying DOS is composed of s - and p -like states with a larger bandwidth (low m_{DOS}^*), rather than half- and full-Heusler compounds, where usually a much larger doping concentration is required due to the more localized nature of the d orbitals building up the DOS (high m_{DOS}^*). At this point, we also note that, interestingly, $S(n)$ first decreases and then increases with n for n -type Ru₂Ti_{1-x}Ta_xSi reported in Ref. [28], instead of monotonically decreasing. While this might be within the margin of experimental uncertainties, it could also be an indication of the contribution of a second conduction band as E_F is shifted further towards higher energies with increasing Ta substitution. Indeed, this would be consistent from a purely rigid-band-like shift of E_F , considering the DOS presented in Fig. 2(b), which changes its slope around $0.4\text{--}0.5 \text{ eV}$ above E_F .

B. Detailed analysis of p - and n -doped Ru₂TiSi

Next, we present a detailed analysis of the temperature-dependent transport properties of n -type

Ru₂Ti_{1-x}Ta_xSi from Ref. [28] and p -type Ru₂TiSi_{1-x}Al_x from this work. Fig. 4(a) displays $S(T)$ data of the former, collected by Fujimoto *et al.* in the temperature range 300–1000 K. Least-squares fits using the 2PB model are again able to reasonably well reproduce all measured curves. Particularly striking is the distinct maximum in $S(T)$ at 700 K, followed by a sign reversal of $S(T)$ at around 900 K for Ru₂Ti_{0.97}Ta_{0.03}Si. This is a direct signature of the strong electron–hole asymmetry and the much higher mobility of holes compared to the conduction band electrons. This is directly reflected in the weighting parameter ϵ_m derived from our fit. A large ϵ_m implies that either a much larger degenerate set of hole pockets (compared to the electron pockets) contributes to the transport properties and/or that conduction band electrons are much heavier compared to the hole-type carriers. An extraordinarily large value of $\epsilon_m \approx 60$ is found for Ru₂Ti_{0.97}Ta_{0.03}Si (and even larger values are found for higher Ta concentrations, see Appendix C), which is especially remarkable, considering that $N_{\text{VB}} = N_{\text{CB}} = 3$ is derived from band structure calculations provided in the Materials Project open web database [47]. We attribute this extreme electron-hole asymmetry to the very dispersive valence band and the much more localized and heavy conduction band states, approximately 0.5 eV above E_F (see Fig. 2(b)). These states become likely important at elevated temperatures and higher doping concentrations, which explains why

a much smaller band asymmetry $\epsilon_m \approx 3.3$ is derived from the analysis of the doping-dependent Seebeck coefficient of Ru₂TiSi-based compounds at 300 K, shown in Fig. 3(b). Nonetheless, this band asymmetry is likely critical for the thermoelectric performance of Ru₂TiSi, which peaks at much higher temperatures $T > 300$ K.

The notion of much lighter holes compared to the conduction electrons is also confirmed when examining the temperature-dependent Seebeck coefficient of p -type Ru₂TiSi_{1-x}Al_x in Fig. 4(b). Both, the experimental data collected in this study and the 2PB model extrapolating towards higher temperatures, show a much broader maximum of $S(T)$, almost saturating at high temperatures. This demonstrates that the weighted contribution of the minority carriers, activated at high temperatures is small. Fig. 4(c) and (d) display the temperature- and composition-dependent weighted mobility μ_W , calculated via the scheme presented in Ref. [48]. Despite the limitations of such an analysis with respect to μ_W owing to (i) bipolar transport and (ii) the rather complex band structure, particularly concerning the conduction band states, it is nonetheless obvious that μ_W is several times larger for p -doped Ru₂TiSi, as opposed to the n -doped compounds reported previously [28].

C. Assessing optimal thermoelectric performance

To evaluate the optimal performance of p - and n -type Ru₂TiSi, we modeled the composition-dependent power factor and thermal conductivity and the maximum zT was estimated based on these theoretical results. Fig. 5(a) shows the carrier doping-dependent PF at 300 K and 700 K. Despite some limitations, our 2PB model traces the trend of the experimental data fairly well and correctly reproduces the enhanced performance of the p -type compounds. The electronic part of the thermal conductivity was calculated via the Wiedemann-Franz law, following the same procedure described in Ref. [22]. The lattice thermal conductivity κ_L , shown in Fig. 5(b), can be described by a simple alloy scattering model [22], which considers two primary scattering contributions, namely, (i) Umklapp phonon-phonon scattering and (ii) scattering of high-frequency phonons with point defects introduced by the random substitution of other atoms in the compound. The latter depends on mass and volume fluctuations and is especially significant when substituting heavy $5d$ elements, *e.g.* Ta instead of Ti. Following this argument, one may assume that other $5d$ elements with similar atomic mass and size, such as Hf, would have a similar effect and composition dependence of κ_L , which is indeed what is observed in Fe₂VAL fH compounds as well [49]. According to the Materials Project database, Ru₂HfSi is also a theoretically predicted stable Heusler compound, as is Ru₂ZrSi, both with a very similar electronic structure to Ru₂TiSi. This suggests that alloying of Ru₂TiSi with Ru₂ZrSi and Ru₂HfSi could be possible, consequently leading to re-

duced κ_L , and hence increased zT . Since the valence band states of full-Heusler compounds, such as Fe₂VAL and Ru₂TiSi, are almost exclusively governed by the X atoms, introducing disorder at the Y site hardly affects the electronic transport properties and retains high values of the weighted mobility [22]. On the other hand, the pseudogap states of the conduction band have Y - e_g orbital character, which results in a strong tradeoff between κ_L and μ_W . Thus, substituting heavy $5d$ elements at the Ti site would be especially promising for p -type Ru₂TiSi, where E_F is located in the Ru- t_{2g} valence bands.

Fig. 5(c) shows the theoretical prediction of the doping-dependent zT for an alloy of Ru₂TiSi and Ru₂HfSi from our 2PB model, assuming similar electronic transport. Darker colors refer to a 20% Ti-Hf substitution, while the lighter colors refer to a 50% alloy, minimizing the lattice thermal conductivity of the compound. For the Ru₂Ti_{0.5}Hf_{0.5}Si alloy, our calculations predict a high maximum $zT = 1 - 1.2$ at 700 K for optimal doping, which motivates experimental exploration of this virgin material platform and showcases that not only half-Heusler but also full-Heusler compounds bear the potential for competitive thermoelectric performance.

IV. CONCLUSIONS

Summarizing, we have investigated thermoelectric transport of Ru₂TiSi-based full-Heusler compounds and compared their transport properties to those of Fe₂VAL. A two-parabolic band model accurately captures the temperature- and doping-dependent thermoelectric transport properties of Ru₂TiSi. The resulting effective band structure underlies that the valence band electronic structure displays much greater potential for realizing high thermoelectric performance compared to p -type Fe₂VAL. Moreover, we predict that p -type Ru₂TiSi would outperform n -type compounds, studied previously, by a factor of 2–3, potentially realizing $zT > 1$ at 700 K upon appropriate reduction of the lattice thermal conductivity, *e.g.*, by isovalent substitution with Zr or Hf at the Ti site. Our work encourages further investigation of the vast phase space of full-Heusler next to half-Heusler compounds as thermoelectric materials.

ACKNOWLEDGMENTS

F.G., M.P., E.B. and T.M. were financially supported by the Japan Science and Technology Agency (JST) program MIRAI, JPMJMI19A1. A.P. acknowledges support from OeAD WTZ (Project CZ 08/2023).

APPENDIX A: STRUCTURAL PROPERTIES

The structural properties and phase purity of p -type Ru₂TiSi_{1-x}Al_x Heusler compounds, synthesized and in-

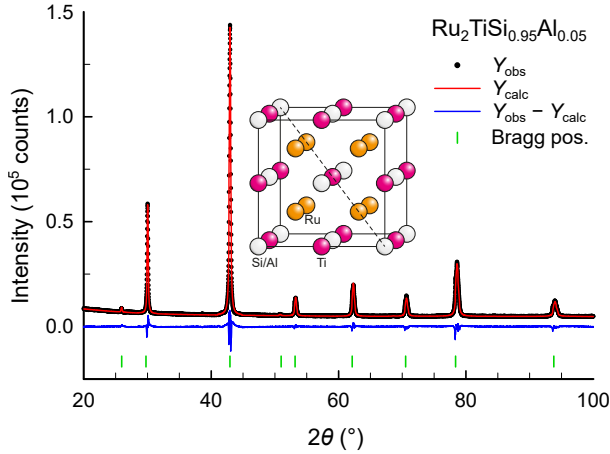


FIG. 6. X-ray powder diffraction pattern of phase-pure p -type $\text{Ru}_2\text{TiSi}_{0.95}\text{Al}_{0.05}$ alongside Rietveld refinement. Inset shows the full-Heusler crystal structure.

investigated in this work, have been studied using x-ray powder diffraction (XRPD) making use of a commercially available diffractometer (AERIS by PANalytical). $\text{Cu-K}\alpha$ radiation has been used and measurements were conducted in a Bragg-Brentano geometry. An exemplary XRPD pattern for the sample with the largest amount of Al substitution, *i.e.* $\text{Ru}_2\text{TiSi}_{0.95}\text{Al}_{0.05}$, is shown in Fig. 6 together with Rietveld refinements, which have been performed using the program PowderCell. The powder pattern displays a single full-Heusler (L2_1) phase with a lattice parameter $a \approx 0.5967$ nm derived from the refinement. The room-temperature lattice parameter is only about 0.14% larger than that of pristine Ru_2TiSi [28], which aligns with expectations since the atomic radii of Si ($r_{\text{Si}} \approx 111$ pm) and Al ($r_{\text{Al}} \approx 125$ pm) are quite similar.

APPENDIX B: ELECTRICAL RESISTIVITY

Fig. 7 summarizes the temperature-dependent electrical resistivity $\rho(T)$ of the Ru_2TiSi system. First, $\rho(T)$ of pristine Ru_2TiSi from Ref. [28] is compared with $\rho(T)$ of pristine Fe_2VAl from Ref. [25] in Fig. 7(a). Despite the larger band gap, evident from the larger Seebeck coefficient of Ru_2TiSi , the resistivity at low temperatures is actually lower compared to Fe_2VAl . We attribute the fact, that Ru_2TiSi is intrinsically doped, with E_{F} located about 0.06 eV below the valence band edge. Thus, at low temperatures $\rho(T)$ should show metallic-like behavior, as is indeed observed. Fujimoto *et al.* reported a carrier mobility of around $100 \text{ cm}^2 \text{ V}^{-1} \text{ s}^{-1}$ for pristine Ru_2TiSi [28], about an order of magnitude larger than that of Fe_2VAl . The carrier mobility in undoped Fe_2VAl is not only smaller due to less dispersive bands at E_{F} , but also hampered by pivotal carrier scattering off localized in-gap impurity states arising from intrinsic Fe/V and Fe/Al exchange antisite defects [50]. It is possible that the formation of such antisite defects, involving the

Ru sublattice is suppressed in Ru_2TiSi due to the larger atomic size mismatch between Ru and Ti/Si, as opposed to Fe versus V/Al.

Fig. 7(b) shows $\rho(T)$ for various n - and p -doped Ru_2TiSi -based fHs from Ref. [28] and this work, respectively. It is evident, that for p -type compounds, $\rho(T)$ decreases extremely quickly, again reflecting the dispersive nature of the valence band electronic structure. For $\text{Ru}_2\text{TiSi}_{1-x}\text{Al}_x$, an Al substitution of only $x = 0.05$, yields a very strong decrease of the room-temperature resistivity down to only $56 \mu\Omega \text{ cm}$, which is comparable to that of ordinary metals.

APPENDIX C: FIT PARAMETERS

Table I lists the obtained fit parameters from our analysis of the temperature-dependent Seebeck coefficient of n -type $\text{Ru}_2\text{Ti}_{1-x}\text{Ta}_x\text{Si}$ from Ref. [28] and p -type $\text{Ru}_2\text{TiSi}_{1-x}\text{Al}_x$ from this work. There are three independent fit parameters that can be extracted to develop an effective band structure model. The first parameter, ϵ_m serves as a weighting parameter, which represents the weighted contribution between the two bands. The larger ϵ_m , the smaller the weighted contribution of the conduction band carriers. Since $m_{\text{VB}} \approx 1 m_e$ could be derived from the carrier concentration dependence of S and because $N_{\text{VB}} = N_{\text{CB}} \approx 3$, ϵ_m can be considered the effective mass of the conduction band electrons $\epsilon_m \sim m_{\text{CB}}$. Taking a look at the values in Table I, it is clear that m_{CB} dramatically increases with Ta substitution, and sort of saturates at very large values of several hundred times the free electron mass (left axis in Fig. 8(a)). This aligns with the notion of a second, much heavier conduction band, further above E_{F} , which is also observed in Fe_2VAl and similar Heusler compounds and whose origin

TABLE I. Obtained fit parameters from modelling the temperature-dependent Seebeck coefficient of $\text{Ru}_2\text{Ti}_{1-x}\text{Ta}_x\text{Si}$ and $\text{Ru}_2\text{TiSi}_{1-x}\text{Al}_x$. The values of Fermi energy are given with respect to the valence/conduction band edge for p - and n -type samples respectively.

Sample	x	ϵ_m	E_{g} (eV)	E_{F} (eV)
n -type $\text{Ru}_2\text{Ti}_{1-x}\text{Ta}_x\text{Si}$	0	1.2	0.24	-0.06
	0.03	62	0.42	0.09
	0.06	392	0.67	0.11
	0.12	385	0.78	0.11
	0.20	239	0.74	0.12
p -type $\text{Ru}_2\text{TiSi}_{1-x}\text{Al}_x$	0	1.2	0.24	-0.06
	0.001	3.4	0.18	-0.05
	0.003	2.1	0.16	-0.08
	0.005	1.5	0.11	-0.09
	0.05	-	-	-0.26

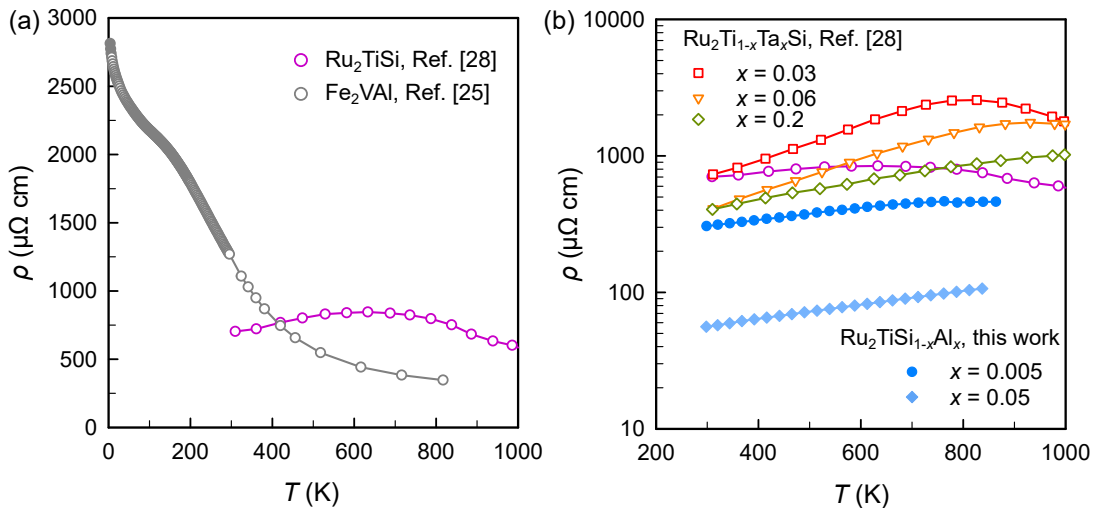


FIG. 7. **Temperature-dependent electrical resistivity of Ru_2TiSi Heusler compounds.** (a) Temperature-dependent electrical resistivity of pristine Ru_2TiSi [28] compared to that of pristine Fe_2VAl [25]. Although Ru_2TiSi has a larger band gap, the electrical resistivity, especially at low temperatures, is lower than that of Fe_2VAl , highlighting that E_F is intrinsically doped in the valence band, which due to its lower effective mass enables a higher carrier mobility and lower resistivity for Ru_2TiSi . (b) Temperature-dependent resistivity for different n - and p -doped Ru_2TiSi samples from Ref. [28] and this work, respectively. It is evident that for p -type $\text{Ru}_2\text{TiSi}_{1-x}\text{Al}_x$, $\rho(T)$ decreases much more rapidly as a function of the doping concentration.

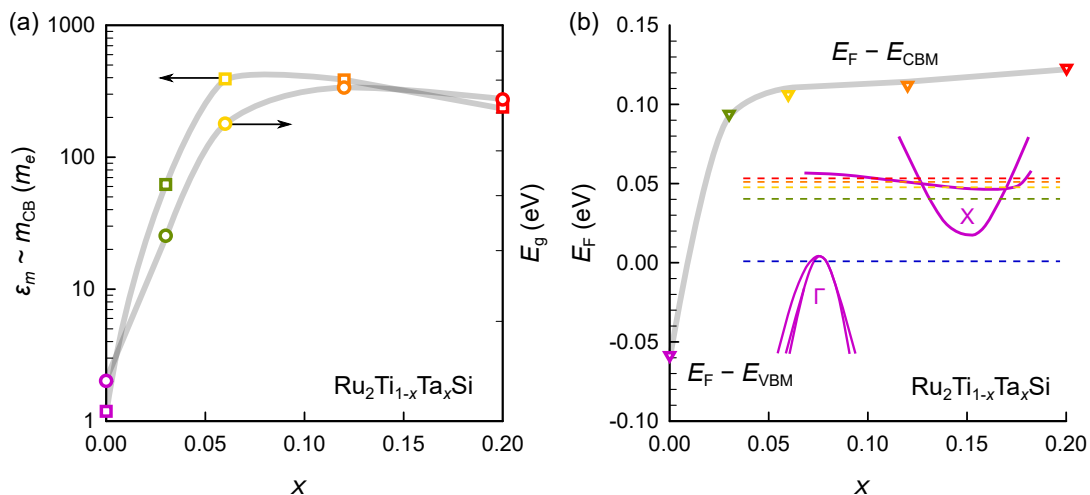


FIG. 8. **Evolution of the electronic structure in n -doped $\text{Ru}_2\text{Ti}_{1-x}\text{Ta}_x\text{Si}$, extracted from fits of the temperature-dependent Seebeck coefficient.** (a) Concentration-dependent weighting parameter ϵ_m (left axis) and band gap E_g (right axis) of n -type $\text{Ru}_2\text{Ti}_{1-x}\text{Ta}_x\text{Si}$. The former corresponds to the effective mass of the conduction band, given that $m_{\text{VB}} \approx 1 m_e$ and $N_{\text{VB}} = N_{\text{CB}}$. Both $\epsilon_m \sim m_{\text{CB}}$ and E_g extracted from our 2PB fits increase with x as E_F is shifted further towards the flat band, located 0.75 eV above the top of the valence bands. (b) Doping level of n -type $\text{Ru}_2\text{Ti}_{1-x}\text{Ta}_x\text{Si}$. E_F abruptly jumps from the valence band towards the conduction band but saturates with increasing x due to the high DOS of the flat-band states.

has been extensively discussed by Bilc *et al.* [51]. Similarly, the band gap derived from our 2PB model seemingly increases with x and saturates around 0.7 – 0.8 eV (right axis in Fig. 8(a)). We interpret this as the position of the second conduction band minimum with respect to the valence band top. The Fermi level E_F , which is given with respect to the top of the valence band for p -type and with respect to the bottom of the conduction band for n -type samples, rapidly jumps from the top of

the valence band and is shifted into the conduction band states. As x increases further, however, E_F almost saturates and is seemingly pinned in the conduction band (see Fig. 8(b)), which is another indirect proof of the flat and heavy band and its associated high DOS that prevents efficient doping (shifts of E_F). A schematic of the effective band structure expected for Ru_2TiSi , the respective energy gaps and position of the Fermi level is presented in Fig. 8(b).

Summarizing, there is conclusive indirect evidence from various fit parameters obtained by modelling the temperature-dependent Seebeck coefficient, that Ru₂TiSi is a narrow-gap semiconductor with dispersive valence and conduction band states and significant electron-hole

asymmetry arising from another conduction band hosting significantly (orders of magnitude) heavier charge carriers, especially when E_F is shifted further into the conduction band via n -type dopants and/or at high temperature where the Fermi-Dirac distribution broadens and excites states further away from E_F .

-
- [1] T. Graf, C. Felser, and S. S. Parkin, *Progress in Solid State Chemistry* **39**, 1 (2011).
- [2] F. Casper, T. Graf, S. Chadov, B. Balke, and C. Felser, *Semiconductor Science and Technology* **27**, 063001 (2012).
- [3] K. Manna, Y. Sun, L. Muechler, J. Kübler, and C. Felser, *Nature Reviews Materials* **3**, 244 (2018).
- [4] I. Galanakis, P. Dederichs, and N. Papanikolaou, *Physical Review B* **66**, 174429 (2002).
- [5] I. Galanakis, P. Mavropoulos, and P. H. Dederichs, *Journal of Physics D: Applied Physics* **39**, 765 (2006).
- [6] S. Skaftouros, K. Özdoğan, E. Şaşıoğlu, and I. Galanakis, *Physical Review B—Condensed Matter and Materials Physics* **87**, 024420 (2013).
- [7] M. Parzer, F. Garmroudi, A. Riss, S. Khmelevskiy, T. Mori, and E. Bauer, *Applied Physics Letters* **120** (2022).
- [8] M. Parzer, F. Garmroudi, A. Riss, M. Reticcioli, R. Podloucky, M. Stöger-Pollach, E. Constable, A. Pustogow, T. Mori, and E. Bauer, *PRX Energy* **3**, 033006 (2024).
- [9] W. G. Zeier, J. Schmitt, G. Hautier, U. Aydemir, Z. M. Gibbs, C. Felser, and G. J. Snyder, *Nature Reviews Materials* **1**, 1 (2016).
- [10] S. Anand, M. Wood, Y. Xia, C. Wolverton, and G. J. Snyder, *Joule* **3**, 1226 (2019).
- [11] L. Wang, Z. Dong, S. Tan, J. Zhang, W. Zhang, and J. Luo, *Advanced Functional Materials* **32**, 2200438 (2022).
- [12] J. Zhang, Z. Dong, S. Tan, Y. Li, J. Zhang, W. Zhang, and J. Luo, *Materials Today Energy* **27**, 101035 (2022).
- [13] G. J. Snyder and E. S. Toberer, *Nature materials* **7**, 105 (2008).
- [14] T. Zhu, C. Fu, H. Xie, Y. Liu, and X. Zhao, *Advanced Energy Materials* **5**, 1500588 (2015).
- [15] G. Rogl and P. F. Rogl, *Crystals* **13**, 1152 (2023).
- [16] W. Li, S. Ghosh, N. Liu, and B. Poudel, *Joule* (2024).
- [17] V. Pecunia, S. R. P. Silva, J. D. Phillips, E. Artegiani, A. Romeo, H. Shim, J. Park, J. H. Kim, J. S. Yun, G. C. Welch, *et al.*, *Journal of Physics: Materials* **6**, 042501 (2023).
- [18] Y. Nishino, S. Deguchi, and U. Mizutani, *Physical Review B—Condensed Matter and Materials Physics* **74**, 115115 (2006).
- [19] F. Garmroudi, M. Parzer, A. Riss, S. Beyer, S. Khmelevskiy, T. Mori, M. Reticcioli, and E. Bauer, *Materials Today Physics* **27**, 100742 (2022).
- [20] E. Alleno, A. Diack-Rasselio, M. Talla Noutack, and P. Jund, *Physical Review Materials* **7**, 075403 (2023).
- [21] H. Okamura, J. Kawahara, T. Nanba, S. Kimura, K. Soda, U. Mizutani, Y. Nishino, M. Kato, I. Shimoyama, H. Miura, *et al.*, *Physical review letters* **84**, 3674 (2000).
- [22] S. Anand, R. Gurunathan, T. Soldi, L. Borgsmiller, R. Orenstein, and G. J. Snyder, *Journal of Materials Chemistry C* **8**, 10174 (2020).
- [23] B. Hinterleitner, F. Garmroudi, N. Reumann, T. Mori, E. Bauer, and R. Podloucky, *Journal of Materials Chemistry C* **9**, 2073 (2021).
- [24] C.-S. Lue and Y.-K. Kuo, *Physical Review B* **66**, 085121 (2002).
- [25] I. Knapp, B. Budinska, D. Milosavljevic, P. Heinrich, S. Khmelevskiy, R. Moser, R. Podloucky, P. Prenninger, and E. Bauer, *Physical Review B* **96**, 045204 (2017).
- [26] S. Mondal, C. Mazumdar, R. Ranganathan, E. Alleno, P. Sreeparvathy, V. Kanchana, and G. Vaitheeswaran, *Physical Review B* **98**, 205130 (2018).
- [27] S. Mondal, K. Ghosh, R. Ranganathan, E. Alleno, and C. Mazumdar, *Journal of Alloys and Compounds* **961**, 171050 (2023).
- [28] T. Fujimoto, M. Mikami, H. Miyazaki, and Y. Nishino, *Journal of Alloys and Compounds* **969**, 172345 (2023).
- [29] M. Parzer, A. Riss, F. Garmroudi, J. de Boor, T. Mori, and E. Bauer, *arXiv preprint arXiv:2409.06261* (2024).
- [30] E. J. Skoug, C. Zhou, Y. Pei, and D. T. Morelli, *Journal of electronic materials* **38**, 1221 (2009).
- [31] M. Vasundhara, V. Srinivas, and V. Rao, *Physical Review B* **77**, 224415 (2008).
- [32] M. Vasundhara, V. Srinivas, and V. Rao, *Journal of Physics: Condensed Matter* **17**, 6025 (2005).
- [33] C. S. Lue, C. Chen, J. Lin, Y. Yu, and Y. Kuo, *Physical Review B* **75**, 064204 (2007).
- [34] Y. Nishino *et al.*, in *Inst. Phys. Conf. Ser.: Mater. Sci. Eng*, Vol. 18 (2011) p. 142001.
- [35] M. Mikami, K. Ozaki, H. Takazawa, A. Yamamoto, Y. Terazawa, and T. Takeuchi, *Journal of electronic materials* **42**, 1801 (2013).
- [36] H. Nakayama, N. Ide, and Y. Nishino, *Materials transactions* **49**, 1858 (2008).
- [37] Y. Terazawa, M. Mikami, T. Itoh, and T. Takeuchi, *Journal of electronic materials* **41**, 1348 (2012).
- [38] M. Mikami, Y. Kinemuchi, K. Ozaki, Y. Terazawa, and T. Takeuchi, *Journal of Applied Physics* **111**, 093710 (2012).
- [39] H. Kato, M. Kato, Y. Nishino, U. Mizutani, and S. Asano, *Nippon Kinzoku Gakkaishi (1952)* **65**, 652 (2001).
- [40] Y. Sandaiji, N. Ide, Y. Nishino, T. Ohwada, S. Harada, and K. Soda, *Funtai Oyobi Funmatsuyakin* **57**, 207 (2010).
- [41] W. Lu, W. Zhang, and L. Chen, *Journal of Alloys and Compounds* **484**, 812 (2009).
- [42] B. Hinterleitner, P. Fuchs, J. Rehak, F. Garmroudi, M. Parzer, M. Waas, R. Svagera, S. Steiner, M. Kishimoto, R. Moser, *et al.*, *Physical Review B* **102**, 075117 (2020).
- [43] F. Garmroudi, A. Riss, M. Parzer, N. Reumann,

- H. Müller, E. Bauer, S. Khmelevskiy, R. Podloucky, T. Mori, K. Tobita, *et al.*, Physical Review B **103**, 085202 (2021).
- [44] N. Reumann, A. Riss, F. Garmroudi, M. Parzer, J. Kovacevic, T. Mori, and E. Bauer, Physical Review B **106**, 235138 (2022).
- [45] Computational DOS data were taken from the Materials Project open web database [52].
- [46] G. Rogl, F. Garmroudi, A. Riss, X. Yan, J. Sereni, E. Bauer, and P. Rogl, Intermetallics **146**, 107567 (2022).
- [47] The valence band at Γ is triply degenerate and the conduction band comprises sixfold degenerate half-pockets at X, thus, also equaling $N = 3$.
- [48] G. J. Snyder, A. H. Snyder, M. Wood, R. Gurunathan, B. H. Snyder, and C. Niu, Advanced Materials **32**, 2001537 (2020).
- [49] E. Alleno, Metals **8**, 864 (2018).
- [50] F. Garmroudi, M. Parzer, A. Riss, A. Pustogow, T. Mori, and E. Bauer, Physical Review B **107**, L081108 (2023).
- [51] D. I. Bilc, G. Hautier, D. Waroquiers, G.-M. Rignanese, and P. Ghosez, Physical review letters **114**, 136601 (2015).
- [52] A. Jain, S. P. Ong, G. Hautier, W. Chen, W. D. Richards, S. Dacek, S. Cholia, D. Gunter, D. Skinner, G. Ceder, *et al.*, APL materials **1** (2013).